Lipid Isobar and Isomer Imaging Using Nanospray Desorption Electrospray Ionization Combined with Triple Quadrupole Mass Spectrometry

Miranda R. Weigand[1]; Daisy M. Unsihuay Vila[1]; Manxi Yang[1]; Hang Hu[1];Emerson Hernly[1]; Matthew Muhoberac[1]; Shane Tichy[2]; Julia Laskin[1*]

[1] Department of Chemistry, Purdue University, 560 Oval Dr., West Lafayette, Indiana, 47907, United States

[2]Agilent Technologies, 5301 Stevens Creek Blvd, Santa Clara, California 95051, United States

Abstract:

Mass spectrometry imaging (MSI) is widely used for examining spatial distributions of molecules in biological samples. Conventional MSI approaches, in which molecules extracted from the sample are distinguished based on their mass-to-charge ratio, cannot distinguish between isomeric species and some closely-spaced isobars. To facilitate isobar separation, MSI is typically performed using high-resolution mass spectrometers. Nevertheless, the complexity of the mixture of biomolecules observed in each pixel of the image presents a challenge even for modern mass spectrometers with the highest resolving power. Herein, we implement nanospray desorption electrospray ionization (nano-DESI) MSI on a triple quadrupole (QqQ) mass spectrometer for the spatial mapping of isobaric and isomeric species in biological tissues. We use multiple reaction monitoring acquisition mode (MRM) with unit mass resolution to demonstrate the performance of this new platform by imaging lipids in mouse brain and rat kidney tissues. We demonstrate that imaging in MRM mode may be used to distinguish between isobaric phospholipids requiring a mass resolving power of 3,800,000. Additionally, we have been able to image eicosanoid isomers, a largely unexplored class of signaling molecules present in tissues at low concentrations, in rat kidney tissue. This new capability substantially enhances the specificity and selectivity of MSI enabling spatial localization of species that remain unresolved in conventional MSI experiments.

Keywords: isobars, isomers, lipids, eicosanoids, *nano-DESI, mass spectrometry imaging (MSI),triple quadrupole mass spectrometer*

Introduction

Mass spectrometry imaging (MSI) is a powerful technique for studying the localization of molecules in biological samples. The developments of MSI instrumentation and computational tools have enabled impactful applications of this technique in clinical research[1,2], drug discovery[3,4], forensics[5,6], microbiology[7,8], and natural product discovery[9–11]. A typical MSI experiment extracts a complex mixture of biomolecules from various locations on the sample and subsequently analyzes without prior separation. As a result, spatial maps of hundreds of molecules in the sample are generated in a label-free fashion. However, the chemical complexity of biological samples presents significant challenges to conventional MSI approaches due to the presence of isobaric and isomeric species, which often remain unresolved.[12,13] High-resolution mass analyzers and post-ionization separation methods are typically used to eliminate interferences and improve the selectivity of MSI experiments. For example, a 21 Tesla-Fourier transform ion cyclotron resonance (21-T FT-ICR) mass spectrometer combined with matrix assisted laser desorption ionization (MALDI) MSI has been used to resolve closely-spaced phospholipid isobars observed in mouse brain tissue sections using the mass resolving power of 1,600,000.[14] Another strategy involves coupling ion mobility spectrometry with MSI (IM-MSI).[13,15] In these experiments, IM is used to separate analytes observed in each pixel of the image based on their size and shape. IM-MSI has separated both isobaric and some isomeric lipids in biological tissues.[16–19] Despite the significant progress in developing MSI systems with high mass resolving power and high-resolution ion mobility separation, it is still impossible to eliminate all the isomeric and isobaric interferences in MSI experiments.

Alternatively, MSI experiments performed in tandem mass spectrometry (MS/MS) mode have emerged as a strategy to improve the selectivity and enable simultaneous imaging and on-the-fly identification of biomolecules.[20–30] MSI-MS/MS experiments are performed by acquiring MS/MS spectra in each pixel of the image and plotting the abundance of characteristic product ions across the sample to generate spatial distributions of targeted analytes. Most MS/MS imaging experiments reported so far have been performed by acquiring a full MS/MS spectrum in each pixel of the image.[24–30] For example, Trim et al., demonstrated that the use of MALDI-IMS-MS/MS improved the specificity of the imaging experiment by eliminating isobaric inferences to visualize the distribution of a pharmaceutical drug's precursor and product ions.[28] Landgraf et al., performed MALDI-MS/MS experiments on lipids present in spinal cord tissue to demonstrate that diagnostic fragments enable the spatial mapping of lipid isobars.[29]

Although these experiments have been typically limited to a handful of selected analytes, a semi-untargeted MS/MS MSI approach has been demonstrated using nanospray desorption electrospray ionization (nano-DESI) on an Orbitrap instrument. Nano-DESI is an ambient ionization technique based on localized liquid extraction that requires minimal sample pretreatment prior to analysis and enables imaging of biological tissues with a spatial resolution down to 10 μm.[31,32] In nano-DESI, analyte molecules are extracted from the sample into a dynamic liquid bridge and gently ionized by electrospray ionization. The continuous sample extraction and high sensitivity of nano-DESI MSI enabled acquisition of MSI-MS/MS data for 92 *m/z* windows that provided imaging

data for an estimated 300 analytes in the same experiment.[27] These experiments demonstrated imaging of closely-spaced isobaric and isomeric species in mouse uterine tissues.

Several groups have coupled MS/MS imaging with derivatization methods for imaging of isomeric phospholipids. For example, ozone-induced dissociation[33], Paternò-Büchi reaction[34], ultraviolet photodissociation[35], and online photochemical derivation[36] have been successfully coupled with MS/MS imaging. In our studies, we developed an online photochemical derivatization approach for imaging isomeric phospholipids using nano-DESI MSI-MS/MS.[36] Although these experiments were performed using broadband MS/MS acquisition, fragment ions corresponding to different isomeric species could be readily separated using an instrument with unit mass resolution.

Other imaging experiments used specific MS/MS transitions to map the distribution of targeted species in biological samples. In fact, the first MS/MS imaging experiment utilized multiple reaction monitoring (MRM) combined with MALDI on a tandem time-flight (TOF/TOF) MS platform to visualize the spatial distribution and enable unambiguous identification of drugs in tissues.[20] Similarly, single reaction monitoring (SRM) on a linear ion trap MS was employed for the spatial profiling of clozapine in kidney and testis tissue sections using desorption electrospray ionization (DESI).[21] Furthermore, MALDI MS/MS imaging using a triple quadrupole mass spectrometer (QqQ) operated in the MRM mode has been used for drug localization in infected rabbit lung tissues.[22] The MRM acquisition mode on QqQ enables fast and selective targeted analysis of molecules in biological samples. Notably, Lamont et al. have investigated the scanning functions of a QqQ in DESI MSI experiments and concluded that MRM acquisition provides the highest sensitivity for imaging of drugs and lipids in biological tissue sections.[23] The speed, sensitivity, and affordability of QqQ instruments make them particularly attractive platforms for MSI-MS/MS experiments.

Inspired by these developments, we have implemented nano-DESI MSI on a QqQ instrument for the spatial mapping of isobaric and isomeric lipid species in biological tissue samples using the MRM acquisition mode. We demonstrate the advantages of MSI-MRM on a QqQ with unit mass resolution for imaging closely-spaced isobaric lipids that cannot be separated using most commercially available high-resolution mass spectrometers. For example, we use the MRM mode on a QqQ to separate lipid isobars that require a mass resolving power of 3,860,000. Furthermore, we use high sensitivity of MRM acquisition on a QqQ for imaging of low-abundance eicosanoid isomers in biological tissues. Our results demonstrate that nano-DESI MSI QqQ is a fast, sensitive, selective, and cost-effective platform for MS/MS imaging of isobaric and isomeric molecules in biological tissue samples.

Experimental Section

Chemical and Solvent Preparation

Omnisolv LC-MS grade water and methanol were purchased from Millipore Sigma (Burlington, MA). Lysophosphotidylethanolamine (LPE) 17:1, phosphatidylcholine (PC) 25:0, and phosphatidylethanolamine (PE) 31:1 lipid standards were purchased from Avanti Polar Lipids (Alabaster, AL). We used 9:1 MeOH:H_2O (v/v) containing 1.5 μM of PC 25:0 and PE 31:1 lipid

standards as the working solvent for positive mode analysis. For negative ion mode experiments, we used 9:1 MeOH:H_2O (v/v) containing 1 μM of LPE 17:1 standard.

Tissue Preparation

Fresh frozen brains of 5-7 months old C57BL/6 female mice were provided by Dr. Chopra's group at Purdue University. Wistar Hannover rat kidney tissues were purchased from BioIVT (Westbury, NY). The brain and kidney tissues were sectioned to 18 μm at −21 °C using a CM1850 Cryostat (Leica Microsystems, Wetzlar, Germany) and thaw mounted onto glass microscope slides (IMEB, Inc Tek-Select Gold Series Microscope Slides, Clear Glass, Positive Charged). Optical images of tissue sections were acquired using a PathScan Enabler IV, pathology slide scanner (Meyer Instruments, Houston, TX). All sections were stored in a −80 °C freezer prior to nano-DESI MSI analysis.

Nano-DESI analysis

Individual line scans and MRM mode imaging experiments were performed on an Agilent Ultivo triple quadrupole mass spectrometer (Agilent, Santa Clara, CA) using a custom-designed nano-DESI source. The source is mounted on a mobile cart positioned in front of the instrument as described previously.[37] Images of the nano-DESI system arranged on a mobile cart are shown in **Figs. 1A and 1B**. The cart holds all components including (1) an optical breadboard for mounting the nano-DESI source components, (2) a lock-in amplifier for the shear force measurement, (3) a computer to control the nano-DESI system, (4) an XYZ-stage for mounting the sample, (5) a glass slide sample holder, (6) micro positioners for the nano-DESI probe, (7) a nano-DESI probe, (8) a stainless steel capillary extension of the heated inlet (50 mm x OD 1.59 mm x ID 0.75 mm, MilliporeSigma, Burlington, MA), and (9) two Dino-Lite (AnMo Electronics Corp., Taiwan) cameras. A pulse of 5 V to 0 V provided by a Multifunction I/O device (National Instruments Corp., Austin, TX) to trigger data acquisition synchronizes the XYZ-stage and Agilent's acquisition software. The commercial source is removed to interface the nano-DESI source with the instrument and a stainless-steel capillary extension is fitted onto the spray shield plate at the mass spectrometer inlet. The extension is sealed against and is in electrical contact with the front of the heated glass capillary of the instrument. The nano-DESI probe is composed of the primary and nanospray fused silica capillaries (OD 150 μm x ID 50 μm Polymicro capillary tubing, Molex, Lisle, IL) positioned relative to each other and instrument inlet using high-resolution micromanipulators (XYZ500TIM, Quater Research and Development, Bend, OR).

In a typical experiment, the extraction solvent is propelled through the primary capillary using a syringe pump (KD Scientific Inc., Holliston, MA). A liquid bridge is formed at the interface of the nano-DESI probe and sample surface. Analytes are desorbed into the liquid bridge, transferred through the nanospray capillary, and ionized at the mass spectrometer inlet. The syringe needle is grounded and a high voltage of is applied to the front section of the heated glass capillary to generate charged analytes using electrospray ionization. A third fused silica capillary (200 μm ID, 790 μm OD) pulled to ~20 μm OD using a P-2000 Puller (Sutter instrument, Novato, CA) serves as a shear force probe. The shear force probe controls the distance between the sample and nano-DESI probe as previously described.[38,39] In summary, two piezoelectric ceramic plates (3.8 MHz,

Steiner & Martins, Inc., Doral, FL) are fastened to the shear force probe: the upper plate causes the probe oscillation with a function generator and the bottom plate detects the amplitude of the shear force vibration with a lock-in amplifier (Stanford Research Systems, Sunnyvale, CA). The shear force probe is positioned close to the nano-DES probe using a motorized micromanipulator (XYZ500MIMT, Quater Research and Development, Bend, OR). Two Dino-Lite microscope cameras are used to guide the assembly of the nano-DESI and shear force probes.

Nano-DESI MSI experiments were performed using 9:1 MeOH:H_2O (v/v) containing lipid standards as a working solvent. The solvent was propelled through the primary capillary using the syringe pump at 0.5 µL/min. Ionization in positive mode was achieved by applying a 3.2 kV potential to the heated inlet extension. Negative ionization was achieved by applying a -3.2 kV potential to the extension. The heated capillary inlet was held at 275°C. The MRM acquisition mode was used to target specific transitions of diagnostic product ions from a selected precursor ion. MRM dwell times were 5 ms per transition with a collision energy of 30 eV. The isolation window for each precursor was 0.7 amu. For imaging of coronal mouse brain and rat kidney sections, data were acquired by scanning the sample under the nano-DESI probe in lines at a scan rate of 40 µm/s while acquiring MRM data and stepping between the lines by 150 µm. The resulting ion images have an average pixel size of 40 µm x 150 µm. For imaging of the mouse cerebellum tissue, data were acquired by scanning the sample under the nano-DESI probe in lines at a scan rate of 20 µm/s while acquiring MRM data and stepping between the lines by 30 µm. The resulting ion images have an average pixel size of 20 µm x 30 µm. The MRM transitions used in this study are listed in **Tables S1** and **S2**. These transitions were chosen based on product ions observed in data-dependent MS/MS spectra of molecules extracted from similar tissue sections acquired using higher-energy collision-induced dissociation (HCD) on a Q-Exactive HF-X Orbitrap mass spectrometer (Thermo Fisher Scientific, Waltham, MA). The HCD spectra were acquired using a mass isolation window of 0.5 *m/z* and HCD energy of 30 arbitrary units specific to the instrument.

For comparison with the results obtained in the MRM mode, several imaging experiments were performed in a conventional, full MS mode using an Agilent 6560 IM-QTOF mass spectrometer as described in our previous study.[37] Details of these experiments are provided in the supplemental information.

Data Analysis

Each line scan was acquired as an individual Agilent raw data file (.d file format) using Agilent MassHunter Workstation software. Data processing was performed using a Python code developed by our group (https://github.com/LabLaskin/MSI-image-generator). The code facilitated the extraction of chromatograms for each MRM transition in every line scan by using the multiplierz Python package. To obtain evenly spaced pixels, the start and end times of each line scan were normalized, followed by nearest-neighbor interpolation. Ion images were constructed by plotting ion abundances of the MRM transitions as function of the location on the tissue as determined by the time-point of each scan. Normalization to internal standards was performed by dividing the endogenous target analyte's MRM transition ion image by the lipid standard's corresponding MRM transition.

Results and Discussion

In this study, we implement nano-DESI MSI on a QqQ instrument and demonstrate its performance by mapping the spatial distributions of closely-spaced isobaric lipids in mouse brain and low-abundance isomeric eicosanoids in rat kidney tissue sections. The experimental workflow of nano-DESI MSI-MRM experiments on a QqQ is illustrated in **Fig. 1C.** Nano-DESI imaging is performed by scanning the sample under the probe at a constant scan rate while acquiring MRM data on a QqQ. The acquisition is performed by sequential isolation and fragmentation of user-defined precursor ions summarized in **Tables S1** and **S2** with an isolation window of 0.7 amu and dwell times of 5 ms. For data processing, we have developed a Python code to efficiently filter data for each MRM transition and generate ion images for each targeted species by plotting the signal in a specific MRM channel as a function of location of the tissue sample. This approach enables the generation of 2-dimensional ion images, in which each pixel corresponds to the abundance of a selected MRM transition. These ion images provide a visual representation of the spatial distribution and abundance of the targeted endogenous analytes within the sample.

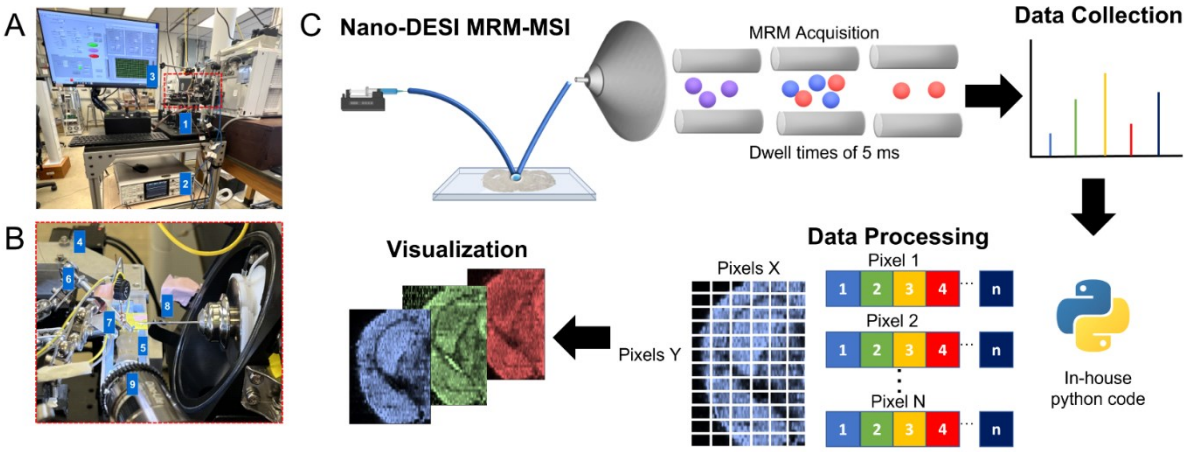

Fig. 1. (A) A photograph of the nano-DESI imaging platform of the custom-designed cart that has components 1) platform for the nano-DESI source, 2) a lock-in amplifier, and 3) a computer that controls system. (B) A zoomed-in photograph corresponding to the red dashed box in panel A includes, 4) the xyz-stage, 5) glass slide sample holder, 6) micro positioners, 7) nano-DESI probe, 8) stainless steel capillary, and 9) Dino-Lite cameras. (C) Experimental workflow for nano-DESI MSI MRM experiments. Analyte extraction by the nano-DESI probe from a specific location on the sample is coupled to the MRM acquisition mode on QqQ. A custom-designed Python code is used to filter data for each MRM transition. Ion images are generated for each targeted species by plotting the signal in a specific MRM channel as a function of location of the tissue sample enabling visualization of the spatial distribution.

Imaging of phospholipid isobars in mouse brain tissue sections

To evaluate the performance of MRM acquisition for nano-DESI MSI, we performed imaging of isobaric phospholipids in mouse brain tissue, a well-studied tissue used as a model system in this study. For the proof-of-concept experiments, we selected two closely-spaced phospholipid isobars,

the $[M+H]^+$ ion of PC 38:4 at *m/z* 810.6007 and $[M+Na]^+$ ion of PC 36:1 at *m/z* 810.5983, that require a mass resolving power of ~337,000 for separation in MS mode. Additionally, we targeted another pair of phospholipid isobars, $[M+K]^+$ ion of PC 32:1 at *m/z* 770.5097 and $[M+Na]^+$ ion of PE (P-38:6) at *m/z* 770.5095, which require an even higher mass resolving power of ~3,850,000 in MS mode. Prior to nano-DESI MSI MRM experiments, we acquired MS/MS spectra of both precursor ions on the tissue to select the appropriate MRM transitions. MS/MS spectra obtained for *m/z* 810.6 and 770.5 precursors on the Q-Exactive HF-X mass spectrometer are shown in **Figs. S1** and **S2**, respectively. Based on these spectra, we selected characteristic product ions corresponding to headgroup losses. The selected MRM transitions for the PC isobars at *m/z* 810.6 were *m/z* 810.6→147 and 810.6→184, which are characteristic ionic products corresponding to headgroups of $[PC\ 36:1+Na]^+$ and $[PC\ 38:4+H]^+$, respectively. For the $[M+K]^+$ ion of PC 32:1 and $[M+Na]^+$ ion of PE (P-38:6) isobars at *m/z* 770.5, the selected MRM transitions were *m/z* 770.5→163, 770.5→164, and 770.5→727 which correspond to the loss of the potassium adduct of ethyl phosphate from PC, sodium adduct of the PE headgroup, and the neutral loss of ethanolamine from PE, respectively.

The results obtained for a coronal mouse brain tissue section using nano-DESI MSI MRM are shown in **Fig. 2**. An optical image of the mouse brain tissue section is shown in **Fig. 2A**. Distinct regions of interest (ROIs) in this tissue including interbrain, hippocampus, and cerebral cortex are labeled in **Fig. 2A**. Un-normalized ion images of the $[M+H]^+$ ion of PC 38:4 and $[M+Na]^+$ ion of PC 36:1 are shown in **Fig. 2B**. The $[M+H]^+$ ion of PC 38:4 shows a distinct localization to the cerebral cortex and hippocampus regions, whereas the $[M+Na]^+$ ion of PC 36:1 is abundant in the cerebral cortex and interbrain regions. **Fig. 2C** shows ion images of the $[M+K]^+$ ion of PC 32:1 and the $[M+Na]^+$ ion of PE (P-38:6). The $[M+K]^+$ ion of PC 32:1 is localized to the cerebral cortex, while the $[M+Na]^+$ ion of PE (P-38:6) shows an enhanced localization in the cerebral cortex and hippocampus regions. We observed the same localization of PE (P-38:6) using both MRM transitions corresponding to the loss of the cationized PE headgroup (*m/z* 770.5→163) and neutral loss of ethanolamine (*m/z* 770.5→727), as shown in **Fig. 2D**, which validates our approach. The observed spatial distributions for the isobars at *m/z* 810.6, the $[M+H]^+$ ion of PC 38:4 and $[M+Na]^+$ ion of PC 36:1, are consistent with the results obtained in a previous study using MALDI MSI on a 21-T FT-ICR.[14] In that study, both species showed a relatively even distribution across the different regions of the mouse brain tissue with the $[M+H]^+$ ion of PC 38:4 showing a decreased abundance and $[M+Na]^+$ ion of PC 36:1 showing an increased abundance in the interbrain region.[14] To further validate the spatial distribution of the PC 36:1 and PC 38:4, we performed imaging experiments in full MS mode using a comparable tissue section. The results obtained in these experiments for multiple adducts of the same lipid are shown in **Fig. S3**. The spatial distributions of $[M+Na]^+$ and $[M+K]^+$ ions of PC 38:4 shown in **Fig. S3D** exhibit the same pattern observed in the MRM mode for $[PC\ 38:4+H]^+$ (*m/z* 810.6→184) in **Fig. 2B.** Similarly, the spatial distributions of the $[M+K]^+$ and $[M+H]^+$ ions of PC 36:1 shown in **Fig. S3C** are comparable to the localization of the sodium adduct of this lipid observed in the MRM mode (**Fig 2B**). These observations confirm that there is a good correspondence between the spatial distributions of lipids obtained in nano-DESI MSI MRM and traditional full MS mode imaging experiments. Furthermore, a good correspondence between nano-DESI MRM MSI and high-resolution MALDI MSI data indicates

that the MRM acquisition mode used in this study is well-suited for separating closely-spaced isobaric phospholipids in biological tissue sections.[14]

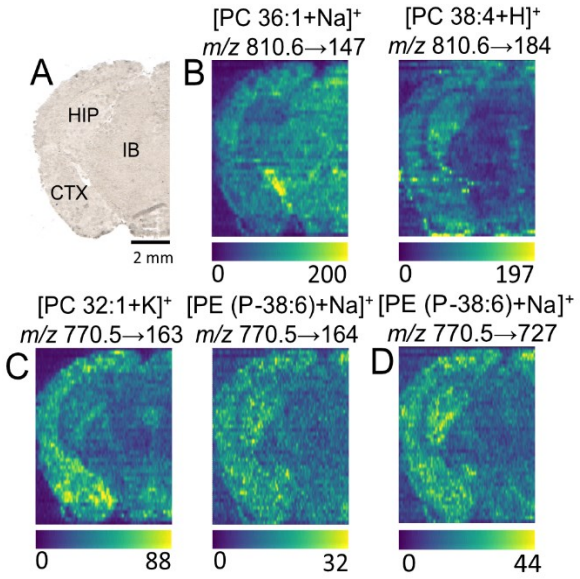

Fig. 2. (A) Optical image of a mouse brain tissue section imaged in positive ion mode. Un-normalized ion images of isobaric (B) $[PC\ 36:1+Na]^+$ (*m/z* 810.6→147) and $[PC\ 38:4+H]^+$ (*m/z* 810.6→184), (C) $[PC\ 32:1+K]^+$ (*m/z* 770.5→163) and $[PE\ (P\text{-}38:6)+Na]^+$ (*m/z* 770.5→164), and (D) $[PE\ (P\text{-}38:6)+Na]^+$ (*m/z* 770.5→164). Regions of interest are labeled for cerebral cortex (CTX), hippocampus (HIP), and interbrain (IB). Scale bar is 2 mm. The maximum ion abundance is shown in the corresponding color bar.

Previous studies have demonstrated that matrix effects resulting from signal suppression during ionization of a complex mixture may affect the accuracy of the measured abundance of endogenous analytes across the tissue sample.[40–42] In MSI experiments, two types of matrix effects have been described: ionization suppression from molecules competing for charge and signal enhancement or suppression attributed to variations in alkali metal concentrations across different regions of the tissue sample.[40–44] Normalizing ion signals to the total ion current (TIC) is commonly used to minimize matrix effects.[43,44] However, in MRM experiments, in which ion abundance is measured within a single *m/z* window per targeted analyte, TIC normalization is no longer applicable. To address this challenge, we explore the use of normalization to standards in nano-DESI MRM experiments to generate ion images free of matrix effects. In these experiments, we used the cerebellum region of mouse brain tissue, in which we expected to observe pronounced matrix effects due to differences in lipid composition in the white and grey matter.[42]

To implement this approach, we introduced the lipid standard, PC 25:0, into the nano-DESI solvent and incorporated MRM transitions for the standard into the MSI-MRM data acquisition workflow. The selected MRM transitions associated with headgroup losses of PC 25:0, were *m/z* 636.5→184, 658.5→147, 674.5→163 corresponding to $[M+H]^+$, $[M+Na]^+$, and $[M+K]^+$ ions, respectively. The optical image of the mouse cerebellum imaged using nano-DESI MSI-MRM is shown in **Fig. 3A.** Un-normalized ion images of endogenous $[PC\ 36:4+H]^+$, $[PC\ 34:1+Na]^+$, and $[PC\ 34:1+K]^+$ are

shown in **Fig. 3B.** The signals of all endogenous PCs are enhanced in the grey matter and suppressed in the white matter. The differential distribution of endogenous PCs can be attributed to the distinct composition of the brain cerebellum, where the white matter is rich in glycolipids and the gray matter has a high abundance of phospholipids.[45–47] Ion signals were then normalized to the appropriate adduct of PC 25:0, shown in **Fig. 3C.** The spatial distribution observed with standard PC 25:0 can be linked to competition for ionization and variations in alkali metal concentrations between the white and grey matter. For example, **Fig. 3D** depicts ion images of the standard $[PC\ 25:0+H]^+$ and $[PC\ 25:0+Na]^+$, which have increased abundances on the glass and suppressed signals on the tissue, whereas $[PC\ 25:0+K]^+$ only appears on the tissue due to a high abundance of potassium in the brain tissue compared to the standard solution. Additionally, all adducts of PC 25:0 are suppressed in the white matter, similar to the endogenous PCs. When corrected for matrix effects, the spatial distribution of $[PC\ 36:4+H]^+$, $[PC\ 34:1+Na]^+$ and $[PC\ 34:1+K]^+$ still have enhanced abundance in the grey matter, but show higher signals in the white matter region compared to the un-normalized images. However, the distribution of $[PC\ 36:4+H]^+$ (**Fig. 3C**) appears nearly uniform across the tissue. This can be attributed to the abundance of alkali salts on the tissue, which leads to competition for ionization between protonated, sodium, and potassium adducts. Our previous study indicated that during nano-DESI MSI the extraction efficiency of endogenous PCs is independent of the brain tissue region.[40] Because both endogenous PCs and the standard PC 25:0 experience similar suppression on the tissue, normalization to the standard effectively compensates for these matrix effects. Additionally, when $[PC\ 34:1+K]^+$ is normalized to $[PC\ 25:0+K]^+$ (**Fig. 3C**), the appearance of signal outside the tissue region becomes apparent due to the absence of $[PC\ 25:0+K]^+$ on the glass side. Nonetheless, even after normalization, the spatial distribution of $[PC\ 34:1+K]^+$ (**Fig. 3B and 3C**) on the tissue remains consistent, with increased abundance in the grey matter region and decreased abundance in the white matter region, as confirmed by the distribution of $[PC\ 34:1+Na]^+$.

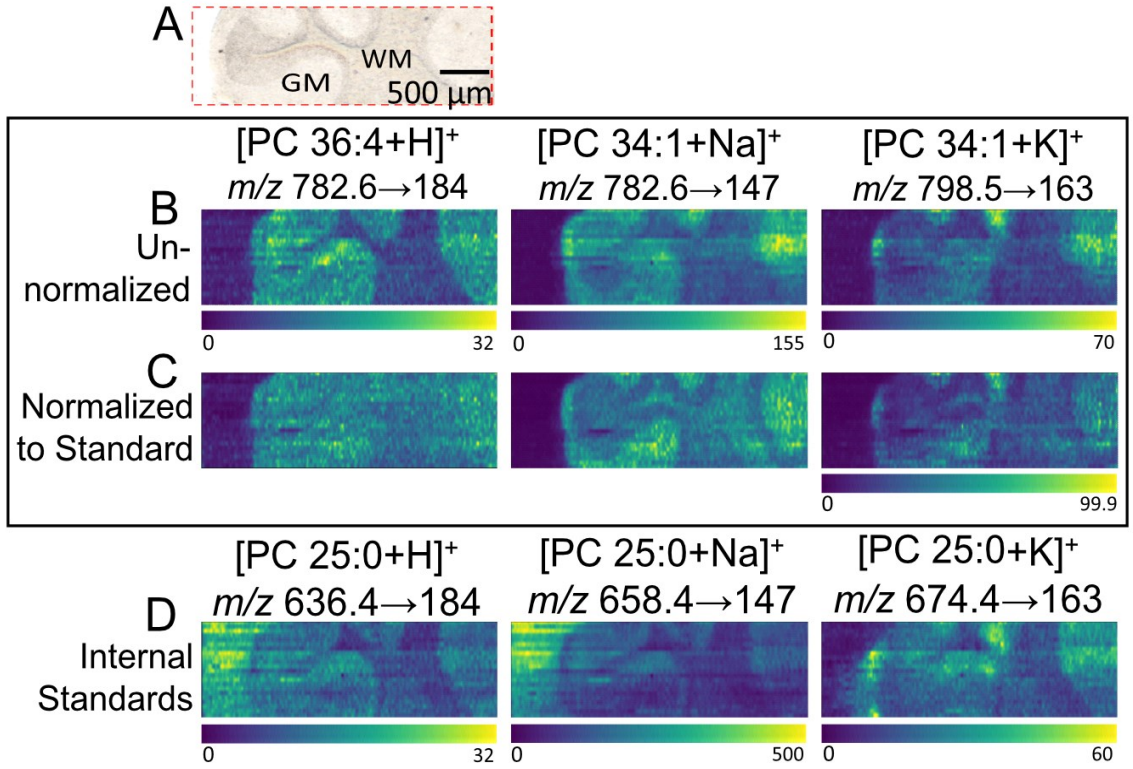

Fig. 3. (A) Optical image of mouse brain cerebellum with labeled areas, GM-grey matter and WM-white matter. Ion images of $[PC\ 36:4+H]^+$ (*m/z* 782.6→184), $[PC\ 34:1+Na]^+$ (*m/z* 782.6→147), and $[PC\ 34:1+K]^+$ (*m/z* 798.5→163) (B) un-normalized and (C) normalized to the internal standard PC 25:0. (D) Un-normalized ion images of the internal standard observed as $[PC\ 25:0+H]^+$ (*m/z* 636.4→184), $[PC\ 25:0+Na]^+$ (*m/z* 658.4→147), and $[PC\ 25:0+K]^+$ (*m/z* 674.4→163). Scale bar is 500 µm. The maximum ion abundance is shown in the corresponding color bar for un-normalized ion images. The normalized ion abundance scale is shown at the 99.9 percentile for the standard normalization ion images.

Imaging of eicosanoid isomers in mouse kidney tissue sections

To demonstrate the MRM acquisition's power for imaging low-abundance isomeric species in biological samples, we investigated the spatial distribution of eicosanoid isomers in rat kidney tissues. Eicosanoids are involved in lipid signaling derived from arachidonic acid (AA) that have important roles in inflammation, cancer, asthma, stroke, and other diseases. Eicosanoids are present in biological tissues at low concentrations ranging from nM to pM. For example, isomers of hydroxyeicosatetraenoic acid (HETE) are present in rat kidney at a level of 1-8 ng/g of tissue.[48] In biological tissues, HETEs are enzymatically derived from arachidonic acid through the lipoxygenase (LOX), cytochrome P-450 (CYP 450), and cyclooxygenase (COX) pathways.[49–51] Each pathway generates different HETE isomers, which are often used as markers of these biochemical pathways.[49–51] The combination of their low abundance and the existence of multiple isomeric HETE species present challenges to visualizing their spatial localization using conventional MSI approaches. The ionization efficiency of HETEs and related oxylipins may be

enhanced through the addition of silver ions to the nano-DESI extraction solvent, which has proven to enhance the ionization of prostaglandins (PGs).[52] Furthermore, silver adduct formation has been utilized to promote structure-specific fragmentation in nano-DESI MSI experiments performed in the MS^3 mode. This approach has enabled the simultaneous imaging and identification of PG isomers.[53] In a previous study, we demonstrated the utility of selected ion monitoring mode for enhancing the sensitivity of nano-DESI MSI for imaging eicosanoids.[54] However, isomeric overlap in MS imaging mode limited the ability to spatially-separate individual isomers, leading to the conclusion that the ion image of HETE obtained in that study was a composite image representing a mixture of HETE isomers present in mouse kidney tissue.

This study demonstrates that MSI performed in the MRM mode enables spatial localization of 11- and 12-HETE isomers in rat kidney tissue. This is achieved using the characteristic MRM transitions of $[M-H]^-$ ions of HETE isomers. Typically, *m/z* 319.2→167 and 319.2→179 MRM transitions corresponding to the cleavage of the carbon-carbon bond adjacent to the hydroxyl group are utilized for the analysis of 11- and 12-HETE, respectively.[55] A negative mode MS/MS spectrum of *m/z* 319.2 acquired in this study directly on an adjacent tissue is shown in **Fig. S4**. The characteristic product ions of 11- and 12-HETE at *m/z* 167 and 179, respectively, are observed in the spectrum and were used as the MRM transitions. The optical image of the rat kidney tissue section is shown in **Fig. 4A** and distinct ROIs including cortex, medulla, and pelvis are highlighted in **Fig. 4B** with blue, red, and green, respectively. Ion images of 11- and 12-HETE generated from *m/z* 319.2→167 and 319.2→179 MRM transitions, respectively, are shown in **Fig. 4C**. Notably, 11-HETE is localized to the cortex and pelvis regions of the rat kidney. Meanwhile, 12-HETE is abundant in the medulla and pelvis regions of the tissue.

The localization of 11-HETE observed in this study is consistent with the known localization of the CYP 450 and COX enzymes that generate this isomer.[49,56] Specifically, the CYP2J enzymes associated with the renal P450 monooxygenase system are known to be expressed in the cortical tubules in rat kidney.[56] Moreover, COX-1 is expressed in the collecting duct of rat kidney, consistent with the localization of 11-HETE in the cortex and pelvis regions.[57] Meanwhile, the localization of 12-HETE to the medulla and pelvis regions is consistent with the known localization of the LOX pathway.[49,50]LOX metabolites, including 12-HETE, are known to be involved in inflammatory responses and affects renal blood flow corresponding with the glomeruli, mesangial cells, and cortical tubules in rat kidney.[50] These proof-of-concept experiments confirm that isomeric overlap is a significant challenge for imaging of HETE isomers and other isomeric eicosanoids in biological tissues.

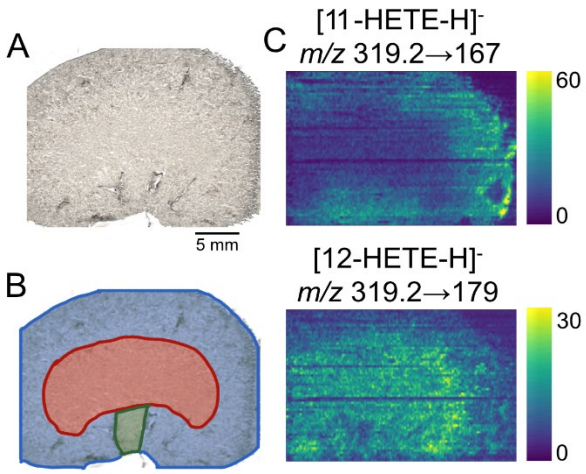

Fig. 4. (A) Optical image of a rat kidney tissue section imaged in negative ion mode. (B) Optical image with highlighted regions of interest including cortex (blue), medulla (red), pelvis (green). (C) Ion images of 11- and 12-HETE obtained using *m/z* 319.2→167 and 319.2→179 MRM transitions, respectively. Scale bar is 5 mm. The maximum ion abundance is shown in the corresponding color bar.

Conclusions

We have successfully implemented nano-DESI MSI on a QqQ and demonstrated the power of this platform for sensitive and selective molecular imaging of endogenous analytes found in biological tissue samples. Using the MRM acquisition mode with unit mass resolution, we efficiently separate both closely-spaced phospholipid isobars and low-abundance eicosanoid isomers in biological tissues. Specifically, we demonstrate imaging of phospholipid isobars in mouse brain tissue that require a mass resolving power of ~3,850,000 in MS acquisition mode. Furthermore, we harness the sensitivity of the MRM acquisition mode on QqQ to obtain first isomer-selective imaging of low-abundance 11- and 12-HETE in rat kidney tissue sections using nano-DESI MSI-MRM. This capability is particularly significant considering the distinct function of eicosanoid isomers in inflammation, cancer, asthma, stroke, and other diseases. This study opens a new and exciting opportunity for MSI-based investigations of the spatial localization of isomeric eicosanoids in biological tissues, providing a more detailed understanding of their role in biological systems. Advantages of MS/MS imaging include the simultaneous spatial mapping and identification of endogenous analytes based on their unique fragmentation patterns or diagnostic fragments. This capability enables the separation of isomeric analytes and eliminates isobaric interferences encountered in traditional imaging approaches. The major limitation of MS/MS imaging is the targeted nature of this approach. We note that the high acquisition rate of MS/MS imaging enabled by the short dwell time used in MRM experiments partially addresses this limitation. In particular, this feature enables the inclusion of numerous *m/z* values of interest while maintaining a reasonably high acquisition speed. The sensitivity of the MRM acquisition mode, resulting from the reduction of the chemical noise, significantly improves the limits of detection and quantitation of biomolecules in imaging experiments. Moreover, MRM imaging on a triple quadrupole mass

spectrometer is one of the most cost-effective strategies for MSI experiments. More broadly, our study has established nano-DESI MSI-MRM as a powerful and cost-effective platform that substantially improves the selectivity of MSI experiments by separating isobaric and isomeric species.

Supporting Information:

Experimental details of imaging experiments performed on the Agilent 6560 IM-QTOF; Lists of the selected MRM transitions for positive and negative ion mode (Table S1 and S2); Full mode ion images (Fig. S3); MS/MS spectra of the lipids displaying characteristic products ions used for MRM transitions (Fig. S1, S2, S4)

Acknowledgements:

The authors gratefully acknowledge the financial support from the Center for Bioanalytical Metrology, an NSF Industry-University Cooperative Research Center (Grant IIP-1916691) and NSF grants 2108729 and 2333734. We are grateful to Agilent for providing in kind the Ultivo QqQ MS used in this study. We thank Palak Manchanda and Prof. Gaurav Chopra (Purdue University) for providing mouse brain tissues.

References

(1) Vaysse, P. M.; Heeren, R. M. A.; Porta, T.; Balluff, B. Mass Spectrometry Imaging for Clinical Research – Latest Developments, Applications, and Current Limitations. *Analyst* **2017**, 142, 2690–2712. https://doi.org/10.1039/C7AN00565B.

(2) Norris, J. L.; Caprioli, R. M. Analysis of Tissue Specimens by Matrix-Assisted Laser Desorption/Ionization Imaging Mass Spectrometry in Biological and Clinical Research. *Chem. Rev.* **2013**, 113, 2309–2342. https://doi.org/10.1021/cr3004295.

(3) Nilsson, A.; Goodwin, R. J. A.; Shariatgorji, M.; Vallianatou, T.; Webborn, P. J. H.; Andrén, P. E. Mass Spectrometry Imaging in Drug Development. *Anal. Chem.* **2015**, 87, 1437–1455. https://doi.org/10.1021/AC504734S.

(4) Lietz, C. B.; Gemperline, E.; Li, L. Qualitative and Quantitative Mass Spectrometry Imaging of Drugs and Metabolites. *Adv. Drug. Deliv. Rev.* **2013**, 65, 1074–1085. https://doi.org/10.1016/j.addr.2013.04.009.

(5) Ifa, D. R.; Manicke, N. E.; Dill, A. L.; Cooks, R. G. Latent Fingerprint Chemical Imaging by Mass Spectrometry. *Science* **2008**, 321, 805. https://doi.org/10.1126/SCIENCE.1157199.

(6) Costa, C.; Jang, M.; De Jesus, J.; Steven, R. T.; Nikula, C. J.; Elia, E.; Bunch, J.; Bellew, A. T.; Watts, J. F.; Hinder, S.; Bailey, M. J. Imaging Mass Spectrometry: A New Way to

Distinguish Dermal Contact from Administration of Cocaine, Using a Single Fingerprint. *Analyst* **2021**, 146, 4010–4021. https://doi.org/10.1039/D1AN00232E.

(7) Watrous, J. D.; Dorrestein, P. C. Imaging Mass Spectrometry in Microbiology. *Nat. Rev. Microbiol.* **2011**, 9, 683–694. https://doi.org/10.1038/nrmicro2634.

(8) Ceglarek, U.; Sickmann, A.; Feucherolles, M.; Frache, G. MALDI Mass Spectrometry Imaging: A Potential Game-Changer in a Modern Microbiology. *Cells* **2022**, 11, 3900. https://doi.org/10.3390/CELLS11233900.

(9) Spraker, J. E.; Luu, G. T.; Sanchez, L. M. Imaging Mass Spectrometry for Natural Products Discovery: A Review of Ionization Methods. *Nat. Prod. Rep.* **2020**, 37, 150–162. https://doi.org/10.1039/C9NP00038K.

(10) Dong, Y.; Aharoni, A. Image to Insight: Exploring Natural Products through Mass Spectrometry Imaging. *Nat. Prod. Rep.* **2022**, 39, 1510–1530. https://doi.org/10.1039/D2NP00011C.

(11) Parrot, D.; Papazian, S.; Foil, D.; Tasdemir, D. Imaging the Unimaginable: Desorption Electrospray Ionization - Imaging Mass Spectrometry (DESI-IMS) in Natural Product Research. *Planta. Med.* **2018**, *84*, 584–593. https://doi.org/10.1055/S-0044-100188.

(12) Rustam, Y. H.; Reid, G. E. Analytical Challenges and Recent Advances in Mass Spectrometry Based Lipidomics. *Anal. Chem.* **2018**, 90, 374–397. https://doi.org/10.1021/ACS.ANALCHEM.7B04836

(13) Rivera, E. S.; Djambazova, K. V.; Neumann, E. K.; Caprioli, R. M.; Spraggins, J. M. Integrating Ion Mobility and Imaging Mass Spectrometry for Comprehensive Analysis of Biological Tissues: A Brief Review and Perspective. *J. Mass. Spectrom.* **2020**, 55, e4614. https://doi.org/10.1002/JMS.4614.

(14) Bowman, A. P.; Blakney, G. T.; Hendrickson, C. L.; Ellis, S. R.; Heeren, R. M. A.; Smith, D. F. Ultra-High Mass Resolving Power, Mass Accuracy, and Dynamic Range MALDI Mass Spectrometry Imaging by 21-T FT-ICR MS. *Anal. Chem.* **2020**, 92, 3133–3142. https://doi.org/10.1021/ACS.ANALCHEM.9B04768.

(15) Sans, M.; Feider, C. L.; Eberlin, L. S. Advances in Mass Spectrometry Imaging Coupled to Ion Mobility Spectrometry for Enhanced Imaging of Biological Tissues. *Curr. Opin. Chem. Biol.* **2018**, *42*, 138–146. https://doi.org/10.1016/J.CBPA.2017.12.005.

(16) Unsihuay, D.; Yin, R.; Sanchez, D. M.; Yang, M.; Li, Y.; Sun, X.; Dey, S. K.; Laskin, J. High-Resolution Imaging and Identification of Biomolecules Using Nano-DESI Coupled to Ion Mobility Spectrometry. *Anal. Chim. Acta.* **2021**, 1186, 339085. https://doi.org/10.1016/J.ACA.2021.339085.

(17) Djambazova, K. V.; Klein, D. R.; Migas, L. G.; Neumann, E. K.; Rivera, E. S.; Van De Plas, R.; Caprioli, R. M.; Spraggins, J. M. Resolving the Complexity of Spatial Lipidomics Using MALDI TIMS Imaging Mass Spectrometry. *Anal. Chem.* **2020**, 92, 13290–13297. https://doi.org/10.1021/ACS.ANALCHEM.0C02520.

(18) Barré, F.; Rocha, B.; Dewez, F.; Towers, M.; Murray, P.; Claude, E.; Cillero-Pastor, B.; Heeren, R.; Porta Siegel, T. Faster Raster Matrix-Assisted Laser Desorption/Ionization

Mass Spectrometry Imaging of Lipids at High Lateral Resolution. *Int. J. Mass. Spectrom.* **2019**, 437, 38–48. https://doi.org/10.1016/J.IJMS.2018.09.015.

(19) Fu, T.; Oetjen, J.; Chapelle, M.; Verdu, A.; Szesny, M.; Chaumot, A.; Degli-Esposti, D.; Geffard, O.; Clément, Y.; Salvador, A.; Ayciriex, S. In Situ Isobaric Lipid Mapping by MALDI–Ion Mobility Separation–Mass Spectrometry Imaging. *J. Mass. Spectrom.* **2020**, 55, e4531. https://doi.org/10.1002/JMS.4531.

(20) Khatib-Shahidi, S.; Andersson, M.; Herman, J. L.; Gillespie, T. A.; Caprioli, R. M. Direct Molecular Analysis of Whole-Body Animal Tissue Sections by Imaging MALDI Mass Spectrometry. *Anal. Chem.* **2006**, 78, 6448-6456. https://doi.org/10.1021/ac060788p.

(21) Wiseman, J. M.; Ifa, D. R.; Zhu, Y.; Kissinger, C. B.; Manicke, N. E.; Kissingera, P. T.; Cooks, R. G. Desorption Electrospray Ionization Mass Spectrometry: Imaging Drugs and Metabolites in Tissues. *Proc. Natl. Acad. Sci. USA.* **2008**, 105, 18120–18125. https://doi.org/10.1073/PNAS.0801066105.

(22) Prideaux, B.; ́roniqueDartois, V.; Staab, D.; Weiner, D. M.; Goh, A.; Via, L. E.; Barry, C. E.; Stoeckli, M. High-Sensitivity MALDI-MRM-MS Imaging of Moxifloxacin Distribution in Tuberculosis-Infected Rabbit Lungs and Granulomatous Lesions. *Anal. Chem.* **2011**, 83, 2112. https://doi.org/10.1021/AC1029049.

(23) Lamont, L.; Eijkel, G. B.; Jones, E. A.; Flinders, B.; Ellis, S. R.; Porta Siegel, T.; Heeren, R. M. A.; Vreeken, R. J. Targeted Drug and Metabolite Imaging: Desorption Electrospray Ionization Combined with Triple Quadrupole Mass Spectrometry. *Anal. Chem.* **2018**, 90, 13229–13235. https://doi.org/10.1021/ACS.ANALCHEM.8B03857

(24) Hansen, R. L.; Lee, Y. J. Overlapping MALDI-Mass Spectrometry Imaging for In-Parallel MS and MS/MS Data Acquisition without Sacrificing Spatial Resolution. *J Am. Soc. Mass. Spectrom.* **2017**, 28, 1910–1918. https://doi.org/10.1007/S13361-017-1699-7

(25) Nilsson, A.; Fehniger, T. E.; Gustavsson, L.; Andersson, M.; Kenne, K.; Marko-Varga, G.; Andrén, P. E. Fine Mapping the Spatial Distribution and Concentration of Unlabeled Drugs within Tissue Micro-Compartments Using Imaging Mass Spectrometry. *PLoS. One.* **2010**, 5, e11411. https://doi.org/10.1371/JOURNAL.PONE.0011411.

(26) Prentice, B. M.; Chumbley, C. W.; Caprioli, R. M. High-Speed MALDI MS/MS Imaging Mass Spectrometry Using Continuous Raster Sampling. *J. Mass. Spectrom.* **2015**, 50, 703–710. https://doi.org/10.1002/JMS.3579.

(27) Lanekoff, I.; Burnum-Johnson, K.; Thomas, M.; Short, J.; Carson, J. P.; Cha, J.; Dey, S. K.; Yang, P.; Prieto Conaway, M. C.; Laskin, J. High-Speed Tandem Mass Spectrometric in Situ Imaging by Nanospray Desorption Electrospray Ionization Mass Spectrometry. *Anal Chem* **2013**, 85, 9596–9603. https://doi.org/10.1021/AC401760S.

(28) Trim, P. J.; Henson, C. M.; Avery, J. L.; McEwen, A.; Snel, M. F.; Claude, E.; Marshall, P. S.; West, A.; Princivalle, A. P.; Clench, M. R. Matrix-Assisted Laser Desorption/Ionization-Ion Mobility Separation-Mass Spectrometry Imaging of Vinblastine in Whole Body Tissue Sections. *Anal. Chem.* **2008**, 80, 8628–8634. https://doi.org/10.1021/AC8015467.

(29) Landgraf, R. R.; Prieto Conaway, M. C.; Garrett, T. J.; Stacpoole, P. W.; Yost, R. A. IMAGING OF LIPIDS IN SPINAL CORD USING INTERMEDIATE PRESSURE MALDI-LIT/ORBITRAP MS. *Anal. Chem.* **2009**, 81, 8488. https://doi.org/10.1021/AC901387U.

(30) Perdian, D. C.; Lee, Y. J. Imaging MS Methodology for More Chemical Information in Less Data Acquisition Time Utilizing a Hybrid Linear Ion Trap-Orbitrap Mass Spectrometer. *Anal. Chem.* **2010**, 82, 9393–9400. https://doi.org/10.1021/AC102017Q.

(31) Yin, R.; Burnum-johnson, K. E.; Laskin, J. High Spatial Resolution Imaging of Biological Tissues Using Nanospray Desorption Electrospray Ionization Mass Spectrometry. *Nat. Protoc.* **2019**, 14, 3445-3470. https://doi.org/10.1038/s41596-019-0237-4.

(32) Laskin, J.; Lanekoff, I. Ambient Mass Spectrometry Imaging Using Direct Liquid Extraction Techniques. *Anal. Chem.* **2016**, 88, 52–73. https://doi.org/10.1021/acs.analchem.5b04188.

(33) Paine, M. R. L.; Poad, B. L. J.; Eijkel, G. B.; Marshall, D. L.; Blanksby, S. J.; Heeren, R. M. A.; Ellis, S. R. Mass Spectrometry Imaging with Isomeric Resolution Enabled by Ozone-Induced Dissociation. *Angew. Chem. Int. Ed.* **2018**, 57, 10530–10534. https://doi.org/10.1002/anie.201802937.

(34) Bednařík, A.; Bölsker, S.; Soltwisch, J.; Dreisewerd, K. An On-Tissue Paternò–Büchi Reaction for Localization of Carbon–Carbon Double Bonds in Phospholipids and Glycolipids by Matrix-Assisted Laser-Desorption–Ionization Mass-Spectrometry Imaging. *Angew. Chem. Int. Ed.* **2018**, 57, 12092–12096. https://doi.org/10.1002/ANIE.201806635.

(35) Klein, D. R.; Feider, C. L.; Garza, K. Y.; Lin, J. Q.; Eberlin, L. S.; Brodbelt, J. S. Desorption Electrospray Ionization Coupled with Ultraviolet Photodissociation for Characterization of Phospholipid Isomers in Tissue Sections. *Anal. Chem.* **2018**, 90, 10100–10104. https://doi.org/10.1021/ACS.ANALCHEM.8B03026.

(36) Unsihuay, D.; Su, P.; Hu, H.; Qiu, J.; Kuang, S.; Li, Y.; Sun, X.; Dey, S. K.; Laskin, J. Imaging and Analysis of Isomeric Unsaturated Lipids through Online Photochemical Derivatization of Carbon–Carbon Double Bonds**. *Angew. Chem. Int. Ed.* **2021**, 60, 7559–7563. https://doi.org/10.1002/ANIE.202016734.

(37) Unsihuay, D.; Yin, R.; Sanchez, D. M.; Yang, M.; Li, Y.; Sun, X.; Dey, S. K.; Laskin, J. High-Resolution Imaging and Identification of Biomolecules Using Nano-DESI Coupled to Ion Mobility Spectrometry. *Anal. Chim. Acta.* **2021**, 1186, 339085. https://doi.org/10.1016/J.ACA.2021.339085.

(38) Nguyen, S. N.; Sontag, R. L.; Carson, J. P.; Corley, R. A.; Ansong, C.; Laskin, J. Towards High-Resolution Tissue Imaging Using Nanospray Desorption Electrospray Ionization Mass Spectrometry Coupled to Shear Force Microscopy. *J. Am. Soc. Mass. Spectrom.* **2018**, 29, 316–322. https://doi.org/10.1007/s13361-017-1750-8.

(39) Lanekoff, I.; Heath, B. S.; Liyu, A.; Thomas, M.; Carson, J. P.; Laskin, J. Automated Platform for High-Resolution Tissue Imaging Using Nanospray Desorption Electrospray Ionization Mass Spectrometry. *Anal. Chem.* **2012**, 84, 8351–8356. https://doi.org/10.1021/ac301909a.

(40) Lanekoff, I.; Thomas, M.; Laskin, J. Shotgun Approach for Quantitative Imaging of Phospholipids Using Nanospray Desorption Electrospray Ionization Mass Spectrometry. *Anal. Chem.* **2014**, 86, 1872–1880. https://doi.org/10.1021/AC403931R.

(41) Bergman, H. M.; Lundin, E.; Andersson, M.; Lanekoff, I. Quantitative Mass Spectrometry Imaging of Small-Molecule Neurotransmitters in Rat Brain Tissue Sections Using Nanospray Desorption Electrospray Ionization. *Analyst* **2016**, 141, 3686–3695. https://doi.org/10.1039/C5AN02620B.

(42) Lanekoff, I.; Stevens, S. L.; Stenzel-Poore, M. P.; Laskin, J. Matrix Effects in Biological Mass Spectrometry Imaging: Identification and Compensation. *Analyst* **2014**, 139, 3528. https://doi.org/10.1039/C4AN00504J.

(43) Rohner, T. C.; Staab, D.; Stoeckli, M. MALDI Mass Spectrometric Imaging of Biological Tissue Sections. *Mech. Ageing. Dev.* **2005**, 126, 177–185. https://doi.org/10.1016/J.MAD.2004.09.032.

(44) Unsihuay, D.; Mesa Sanchez, D.; Laskin, J. Quantitative Mass Spectrometry Imaging of Biological Systems. *Annu. Rev. Phys. Chem*. **2021**, 72, 307–329. https://doi.org/10.1146/annurev-physchem-061020-053416.

(45) Brady, S.; Siegel, G.; Albers, R. W.; Price, D. L.; Brady, S. T.; Siegel, G. J.; Albers, R. W.; Price, D. L. *Basic Neurochemistry : Molecular, Cellular and Medical Aspects*, 7th Ed.; Elsevier Science & Technology: Burlington, United States, 2005.

(46) O'Brien, J. S.; Fillerup, D. L.; Mead, J. F. Quantification and Fatty Acid and Fatty Aldehyde Composition of Ethanolamine, Choline, and Serine Glycerophosphatides in Human Cerebral Grey and White Matter. *J. Lipid. Res.* **1964**, 5, 329–338. https://doi.org/10.1016/S0022-2275(20)40201-9.

(47) O'Brien, J. S.; Sampson, E. L. Fatty Acid and Fatty Aldehyde Composition of the Major Brain Lipids in Normal Human Gray Matter, White Matter, and Myelin. *J. Lipid. Res.* **1965**, 6, 545–551. https://doi.org/10.1016/S0022-2275(20)39620-6.

(48) Aukema, H. M.; Lu, J.; Borthwick, F.; Proctor, S. D. Dietary Fish Oil Reduces Glomerular Injury and Elevated Renal Hydroxyeicosatetraenoic Acid Levels in the JCR:LA-Cp Rat, a Model of the Metabolic Syndrome. *Br. J. Nutr.* **2013**, 110, 11–19. https://doi.org/10.1017/S0007114512004606.

(49) Wang, T.; Fu, X.; Chen, Q.; Patra, J. K.; Wang, D.; Wang, Z.; Gai, Z. Arachidonic Acid Metabolism and Kidney Inflammation. *Int. J. Mol. Sci.* **2019**, 20. https://doi.org/10.3390/IJMS20153683.

(50) Imig, J. D. Eicosanoid Regulation of the Renal Vasculature. *Am. J. Physiol. Renal. Physiol.* **2000**, 279. https://doi.org/10.1152/AJPRENAL.2000.279.6.F965

(51) Buczynski, M. W.; Dumlao, D. S.; Dennis, E. A. An Integrated Omics Analysis of Eicosanoid Biology. *J. Lipid. Res.* **2009**, 50, 1015–1038. https://doi.org/10.1194/JLR.R900004-JLR200.

(52) Duncan, K. D.; Fang, R.; Yuan, J.; Chu, R. K.; Dey, S. K.; Burnum-Johnson, K. E.; Lanekoff, I. Quantitative Mass Spectrometry Imaging of Prostaglandins as Silver Ion

Adducts with Nanospray Desorption Electrospray Ionization. *Anal. Chem.* **2018**, 90, 7246–7252. https://doi.org/10.1021/acs.analchem.8b00350.

(53) Mavroudakis, L.; Lanekoff, I. Identification and Imaging of Prostaglandin Isomers Utilizing MS3 Product Ions and Silver Cationization. *J. Am. Soc. Mass. Spectrom.* **2023**, 34, 2341-2349. https://doi.org/10.1021/jasms.3c00233.

(54) Huffstutler, C. D.; Sanchez, D. M.; Weigand, M. R.; Hu, H.; Li, X.; Chegwidden, A. J.; Nagornov, K. O.; Kozhinov, A. N.; Tsybin, Y. O.; Laskin, J. Multiple Selected Ion Monitoring Mode for Sensitive Imaging of Eicosanoids in Tissues Using Nanospray Desorption Electrospray Ionization (Nano-DESI) Mass Spectrometry. *Int. J. Mass. Spectrom.* **2023**, 491, 117101. https://doi.org/10.1016/J.IJMS.2023.117101.

(55) Sorgi, C. A.; Peti, A. P. F.; Petta, T.; Meirelles, A. F. G.; Fontanari, C.; de Moraes, L. A. B.; Faccioli, L. H. Comprehensive High-Resolution Multiple-Reaction Monitoring Mass Spectrometry for Targeted Eicosanoid Assays. *Sci. Data., **2018,*** 5, 1–12. https://doi.org/10.1038/sdata.2018.167.

(56) Ma, J.; Qu, W.; Scarborough, P. E.; Tomer, K. B.; Moomaw, C. R.; Maronpot, R.; Davis, L. S.; Breyer, M. D.; Zeldin, D. C. Molecular Cloning, Enzymatic Characterization, Developmental Expression, and Cellular Localization of a Mouse Cytochrome P450 Highly Expressed in Kidney. *J. Biol. Chem.* **1999**, 274, 17777–17788. https://doi.org/10.1074/jbc.274.25.17777.

(57) Smith, W. L.; DeWitt, D. L.; Garavito, R. M. Cyclooxygenases: Structural, Cellular, and Molecular Biology. *Annu. Rev. Biochem.* **2000**, 28, 145–182. https://doi.org/10.1146/annurev.biochem.69.1.145.